APL Materials

$LaPr_3Ni_3O_{9.76}$ as a candidate solid oxide fuel cell cathode: Role of microstructure and interface structure on electrochemical performance

Cite as: APL Mater. **7**, 013204 (2019); https://doi.org/10.1063/1.5050249
Submitted: 28 July 2018 . Accepted: 22 October 2018 . Published Online: 11 December 2018

Mudasir A. Yatoo, Ainara Aguadero, and Stephen J. Skinner

View Online Export Citation CrossMark

ARTICLES YOU MAY BE INTERESTED IN

Hydrogen oxidation kinetics on platinum-palladium bimetallic thin films for solid acid fuel cells
APL Materials **7**, 013201 (2019); https://doi.org/10.1063/1.5050093

The role of oxide interfaces in highly confined electronic and ionic conductors
APL Materials **7**, 013101 (2019); https://doi.org/10.1063/1.5052057

Unraveling bulk and grain boundary electrical properties in $La_{0.8}Sr_{0.2}Mn_{1-y}O_{3\pm\delta}$ thin films
APL Materials **7**, 013205 (2019); https://doi.org/10.1063/1.5054576



© 2018 Author(s).

$LaPr_3Ni_3O_{9.76}$ as a candidate solid oxide fuel cell cathode: Role of microstructure and interface structure on electrochemical performance

Cite as: APL Mater. 7, 013204 (2019); doi: 10.1063/1.5050249
Submitted: 28 July 2018 • Accepted: 22 October 2018 •
Published Online: 11 December 2018

View Online Export Citation CrossMark

Mudasir A. Yatoo,[1,2] Ainara Aguadero,[1] and Stephen J. Skinner[1,2,a)]

AFFILIATIONS

[1] Department of Materials, Faculty of Engineering, Imperial College London, Exhibition Road, London SW7 2AZ, United Kingdom
[2] EPSRC Centre for Doctoral Training in Advanced Characterisation of Materials, Exhibition Road, London SW7 2AZ, United Kingdom

[a)] Author to whom correspondence should be addressed: s.skinner@imperial.ac.uk

ABSTRACT

A new higher-order Ruddlesden-Popper phase composition $LaPr_3Ni_3O_{9.76}$ was synthesised by a sol-gel route and studied for potential intermediate-temperature solid oxide fuel cell cathode properties by electrochemical impedance spectroscopy. The focus of the work was optimisation of the microstructure and interface structure to realise the best performance, and therefore symmetrical cells after impedance testing were subsequently studied by scanning electron microscopy for post-microstructural analysis. It was observed that the cathode ink prepared after ball milling the material and then triple roll milling the prepared ink gave the lowest area specific resistance (ASR) of 0.17 Ω cm^2 at 700 °C when a $La_{0.8}Sr_{0.2}Ga_{0.8}Mn_{0.2}O_{3-\delta}$ (LSGM) electrolyte that had been previously polished was used. The post-microstructural studies, as expected, showed an improved interface structure and relatively good particle interconnectivity and much less sintering when compared to the symmetrical half-cells constructed using the ink prepared from the as-synthesised material. The interface structure was further improved significantly by adding a ~10 μm thick LSGM ink interlayer, which was reflected in the electrochemical performance, reducing the ASR of the material from 0.17 Ω cm^2 to 0.08 Ω cm^2 at 700 °C. This is to date the best performance reported for an n = 3 Ruddlesden-Popper phase material with LSGM as the electrolyte.

© 2018 Author(s). *All article content, except where otherwise noted, is licensed under a Creative Commons Attribution (CC BY) license (http://creativecommons.org/licenses/by/4.0/).* https://doi.org/10.1063/1.5050249

One of the key tasks in SOFC development is the lowering of operational temperatures to combat material degradation and hence increase device lifetime.[1] However, at intermediate temperatures (550-750 °C), the oxygen reduction kinetics are reduced and thus negatively impact the performance of the cell. Therefore, the focus is to achieve considerable improvement in cathode oxygen reduction reaction (ORR) kinetics at intermediate temperatures and faster oxygen transport across the electrode/electrolyte interface.[1] A further shortcoming identified has been the limited participation of the triple phase boundary in terms of its area in electronic conducting solid oxide fuel cell (SOFC) electrode materials, and thus mixed ionic and electronic conducting (MIEC) materials are being studied in order to extend the involvement of the electrode in the ORR to realise better performance in SOFCs.[2–4] This outlines the importance of MIEC materials since the extended participation of the electrode in the ORR is expected to compensate for the reduced oxygen reduction kinetics at intermediate temperatures.

One approach in the development of new MIEC electrode materials for SOFCs is to focus on perovskite-related layered oxides. Recent interest has been directed toward the Ruddlesden-Popper (RP) phases. Formulated as $A_{n+1}B_nO_{3n+1}$

© Author(s) 2018

(n = 1, 2, and 3), the RP phases consist of n consecutive ABO_3 perovskite layers, alternating with AO rock-salt layers, stacking along the crystallographic c-axis.[5] The lower-order RP phases, particularly the n = 1 phases such as $La_2NiO_{4+\delta}$, $Pr_2NiO_{4+\delta}$, and $Nd_2NiO_{4+\delta}$,[6–8] have previously been extensively investigated, with studies considering the electronic and ionic transport as well as the performance of these oxides as SOFC electrodes. Higher-order RP phases (n = 3) have received little attention, but because of their excellent total conductivity and improved stability[6,7] in the temperature ranges of interest (550–750 °C) when compared to the n = 1 phases, there is significant potential to develop a new class of electrode.

In developing SOFC cathodes, it is important that discovery of promising new material families and optimisation of existing materials are investigated, particularly focusing on the interfacial characteristics. Oxygen ions produced at the cathode surface have to diffuse through the electrode/electrolyte interface, and depending on the interfacial resistance of the SOFC system, the cell performance could be limited. It is challenging to obtain an atomic-scale picture of the interface during operation because a non-destructive probe with high penetration power and high sensitivity, compatible with the harsh operation conditions, is needed.[9] One approach is to construct cells for electrochemical impedance measurements and follow the measurements with post-measurement microstructural analysis. Using this information, logical steps such as modifying the electrode ink preparation, cell sintering temperatures, modifying the electrolyte surfaces, or adding an interlayer to optimise the interface structure can be systematically studied.

There are many reports in the literature highlighting routes to optimising the interface structure.[10–13] Working on ungraded and functionally graded composites of $La_2NiO_{4+\delta}$ and $La_4Ni_3O_{10-\delta}$, Woolley and Skinner showed the significant role microstructure and electrode/electrolyte contact have on the performance of a material used as an electrode.[12,13] They reported the ASR of 0.62 Ω cm^2 at 700 °C for an ungraded 50:50 composite,[13] which was further improved to 0.53 Ω cm^2 at 700 °C by functional grading of the 50:50 composite cathode.[12] This improved performance in both cases was ascribed to a good combination of ionic and total conductivity, being contributed by two different constituents of the composite and the resulting microstructure and improved electrode/electrolyte interface contact. Vibhu *et al.*, understanding the importance of electrode/electrolyte contact, used a $Ce_{0.9}Gd_{0.1}O_{1.95}$ (GDC) interlayer in their study of another end member of the series, $Pr_4Ni_3O_{10+\delta}$, as an SOFC cathode with yttria stabilised zirconia, ZrO_2-Y_2O_3 (YSZ), as the electrolyte.[10]

Several authors working on related RP materials, $La_3Ni_2O_{7-\delta}$ and $La_4Ni_3O_{10-\delta}$ have explored the development of the microstructure, including preparing infiltrated composite cathodes of these oxides, and reported improvement in performance.[14–17] Choi *et al.* reported an ASR of 0.11 Ω cm^2 at 750 °C for $La_3Ni_2O_7$,[14] and Kim *et al.* reported the ASR of a Sr doped n = 3 phase as ~0.13 Ω cm^2 at 750 °C.[15] Sharma *et al.* by using a spray deposition technique improved the performance for the n = 3 composition $La_4Ni_3O_{10-\delta}$, reporting an ASR of 0.30 Ω cm^2 at 700 °C, whilst producing a composite with $Ce_{0.9}Gd_{0.1}O_{2-\delta}$ improved this ASR by one order of magnitude.[16,17] Earlier studies of $La_4Ni_3O_{10-\delta}$ as an SOFC cathode by Amow and co-workers[7] reported an ASR of 1.0 Ω cm^2 at 800 °C. This significant improvement from 1.0 Ω cm^2 at 800 °C to 0.15 Ω cm^2 at 700 °C was ascribed to the improvement of the cathode microstructure and thereby the adherence of the electrode to the electrolyte pellet. A report by Sharma *et al.*[17] in which the ASR was reported to decrease from 72.41 Ω cm^2 to 12.78 Ω cm^2 and then to 2.21 Ω cm^2 by changing the microstructure from isolated cauliflowers to connected round agglomerates and then to the 3-D coral-type microstructure, respectively, clearly signifies the importance of optimising the microstructure and its influence on the electrochemical performance of these materials. It, however, is also important to point out that it is possible to have comparable oxygen reduction activity even with substantial differences in the microstructure and interface morphology. Jiang, for example, reported no sizeable impact on the electrocatalytic activity by examining the thermally and electrochemically induced electrode/electrolyte interfaces in $La_{1-x}Sr_xMnO_{3-\delta}$ (LSM) and $La_{1-x}Sr_xCo_{1-y}Fe_yO_{3-\delta}$ (LSCF) electrodes on YSZ and GDC electrolytes, respectively.[18]

In this regard, we have recently reported the preparation of a higher-order RP composition, $La_2Pr_2Ni_3O_{9.65}$, and presented preliminary solid oxide fuel cell cathode performance[19] data. An Area Specific Resistance (ASR) of 0.34 Ω cm^2 at 800 °C was reported, and two important observations of poor cathode microstructure and lack of adherence to the electrolyte were noted. More importantly, this previous work highlighted the importance of electrode/electrolyte interface structure in the development of SOFC technology. Building on these previous studies as well as our previous observations of poor cathode microstructure and electrode-electrolyte contact being the reasons behind the relatively lower electrochemical performance of a related composition, $La_2Pr_2Ni_3O_{9.65}$, we report the successful preparation and optimisation of a new RP composition, $LaPr_3Ni_3O_{9.76}$, with impressive electrochemical performance.

$LaPr_3Ni_3O_{9.77}$ (L1P3N3) was synthesised using the citrate sol-gel route. Stoichiometric amounts of $La(NO_3)_3 \cdot 6H_2O$ (Sigma Aldrich, 99.0%), $Pr(NO_3)_3 \cdot 6H_2O$ (Sigma Aldrich, 99.99%), and $Ni(NO_3)_2 \cdot 6H_2O$ (Sigma Aldrich, 99.0%) were dissolved in an aqueous solution of 10% (by weight) of citric acid (Sigma Aldrich, 99.99%). The solution was heated at 250 °C, under constant stirring for three hours, until a gel was obtained. The gel, after being decomposed in air for 12 h at 600 °C, was ground, and the resultant powder was annealed for 24 h in air at 950 °C. The XRD patterns of the material were collected using a PANalytical X'Pert Pro MPD (Cu Kα source), and Rietveld refinement of the XRD data, performed with the GSAS/EXPGUI software package,[20,21] was used to confirm the phase identification and extract unit cell parameters. The

© Author(s) 2018

TABLE I. Summary of the cell preparation conditions for the seven samples investigated.

Sample	Ink	Electrode sintering conditions	Electrolyte	Cell configuration
1	A	1150 °C/1 h	Polished LSGM	L1P3N3/LSGM/L1P3N3
2	B	1150 °C/1 h	As sintered LSGM	L1P3N3/LSGM/L1P3N3
3	B	1150 °C/1 h	Polished LSGM/1000 °C, 6 h	L1P3N3/LSGM/L1P3N3
4	B	1150 °C/1 h	Polished and calcined LSGM	L1P3N3/LSGM/L1P3N3
5	B	1150 °C/1 h, slow cooling	Polished LSGM	L1P3N3/LSGMInk/LSGM/LSGMInkL1P3N3
6	B	1050 °C/1 h, slow cooling	Polished LSGM	L1P3N3/LSGMInk/LSGM/LSGMInkL1P3N3
7	B	1050 °C/2.5 h	Polished LSGM	L1P3N3/LSGMInk/LSGM/LSGMInkL1P3N3

XPS spectra were obtained using a Thermo Scientific K-Alpha + instrument with a monochromatic Al Kα radiation source (hν = 1486.6 eV) operating at 2×10^{-9} mbar base pressure. The X-ray source used a 6 mA emission current and 12 kV anode bias, giving an X-ray spot size of up to 400 μm^2. A pass energy of 200 eV was used for survey spectra and 20 eV for core levels. Avantage Data System software (ThermoFisher Scientific) was used for quantitative analysis, and binding energy values were corrected by setting the C1s peak to 284.8 eV. Post-microstructural investigations of the half-cells were achieved using a LEO Gemini 1525 FEG scanning electron microscope with an accelerating voltage of 5.0 kV.

The commercially available $La_{0.8}Sr_{0.2}Ga_{0.8}Mg_{0.2}O_{3-\delta}$ (LSGM) electrolyte powder, purchased from Fuel Cell Materials, USA, was pressed (0.04 MPa) into 13 mm diameter disks using a uniaxial press, followed by the cold isostatic press (300 MPa), and then sintering at 1450 °C for 8 h. The thickness of the LSGM pellets after sintering and polishing with silicon carbide paper (1200 grit) was in the 700-800 μm range. An L1P3N3 electrode ink was prepared by mixing with an organic ink vehicle supplied by Fuel Cell Materials, USA, in a 2:1 weight ratio to prepare symmetrical cells by a screen-printing technique. Two types of electrode slurries were prepared, one by homogeneously mixing the as-synthesised powders with an

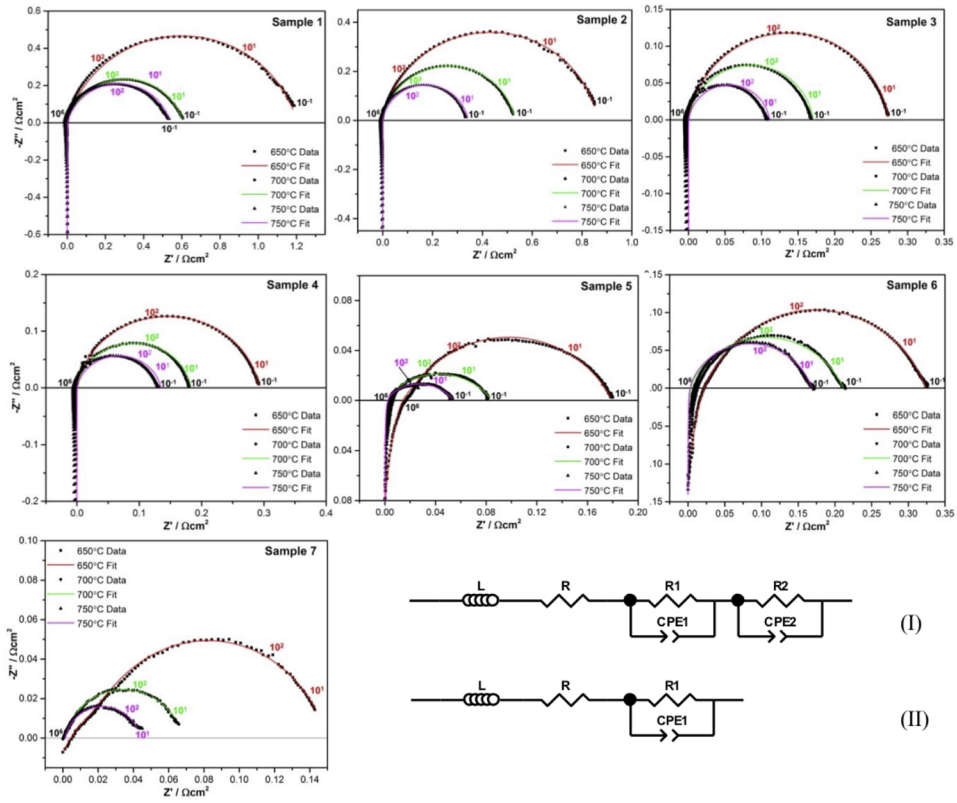


FIG. 1. Nyquist plots recorded for $LaPr_3Ni_3O_{9.76}$ oxygen electrode at 650 °C, 700 °C, and 750 °C. Dotted lines represent the data, and solid lines represent the fit to the equivalent circuits used. At low temperatures, the equivalent circuit (I) used is LR(CPE_1R_1) (CPE_2R_2), and at high temperatures, the equivalent circuit (II) used is LR(CPE1R1).

© Author(s) 2018

ink vehicle (**ink A**) and another by ball milling the powders for 24 h before mixing with an ink vehicle and then triple roll milling the prepared ink to have uniform particle size (>3 μm) (**ink B**).

Symmetrical cells of the configuration L1P3N3||LSGM|| L1P3N3 were prepared by screen-printing ink A on both sides of polished LSGM pellets (**sample** 1) and ink B on both sides of as-sintered LSGM electrolyte pellets (**sample** 2), polished LSGM pellets (**sample** 3), and polished and calcined (1000 °C for 6 h) LSGM pellets (**sample** 4), all with an active area of 0.5 cm^2. **Sample** 5 was prepared in the same way as sample 3 except for the modification of adding an LSGM ink interlayer, which was screen-printed on the LSGM pellet which was then annealed for 1 h at 1000 °C before the L1P3N3 electrode could be screen-printed, leading to the cell configuration of L1P3N3|LSGMInk|LSGM|LSGMInk|L1P3N3. In all the samples described above, cells were sintered at 1150 °C for 1 h to ensure good electrode adherence. Since the L1P3N3 decomposes at temperatures above 1000 °C, slow cooling (0.5 °C/min) to 950 °C from 1150 °C under oxygen was required, which leads to the re-formation of L1P3N3, and to make sure that L1P3N3 is fully recovered, the cell was kept at 950 °C for 6 h. **Sample** 6 was prepared in the same way as that of sample 5, except that the cell sintering was performed at 1050 °C, and **sample** 7 was sintered for 2.5 h at 1050 °C under ambient conditions. A summary of the cell preparation is presented in Table I. A Pt mesh was used as the current collector, and impedance measurement of the half-cells was performed using a Solartron 1260 impedance gain/phase analyzer in combination with a Solartron 1287 electrochemical interface in the 0.1–10^6 Hz frequency range with a perturbation amplitude of 10 mV. DRTtools was used to interpret the impedance spectroscopy data via distribution of relaxation time to identify the processes at low and high frequencies.[22]

X-ray diffraction patterns and XPS spectra, for phase identification and for elemental composition, respectively, both are provided in the supplementary material. The cathode performance obtained by impedance spectroscopy measurements of all of the samples is presented as Nyquist plots, along with the fitting results, in Fig. 1. The equivalent circuit adopted for samples 1-4 is LR(CPE_1R_1), where L is the inductance, R represents the ohmic resistance, and (CPE_1R_1) represents the constant phase element and resistance of the processes occurring at the cathode. In the case of samples 5-7, the Nyquist plot shows two separate responses (high and low frequency responses) at low temperatures, but only one response can be seen at high temperatures (Table II). Accordingly, the equivalent circuit adopted for low temperatures is LR(CPE_1R_1) (CPE_2R_2), whereas the equivalent circuit LR(CPE_1R_1) was used for high temperatures. Since it is difficult to separate and compare the high, medium, and low frequency responses in Nyquist plots above, DRTtools[22] was used to interpret the impedance spectroscopy data in terms of distribution of relaxation times for sample 6 (Fig. 2). Similar behavior was observed in samples 5 and 7. A clear observation of a very small contribution arising from the high-frequency

TABLE II. Low and high frequency contributions to overall polarisation resistance in samples 5-7.

Temperature (°C)		R_H (Ω cm^2)	R_L (Ω cm^2)	R_T (Ω cm^2)		R_H (Ω cm^2)	R_L (Ω cm^2)	R_T (Ω cm^2)		R_H (Ω cm^2)	R_L (Ω cm^2)	R_T (Ω cm^2)
575		0.06	0.74	0.80		0.08	1.10	1.18		0.14	0.61	0.75
600		0.05	0.41	0.47		0.03	0.66	0.69		0.07	0.28	0.35
625	S5	0.02	0.25	0.27	S6	0.01	0.44	0.45	S7	0.03	0.20	0.23
650			0.16	0.16			0.30	0.30		0.01	0.13	0.14
675			0.10	0.10			0.24	0.24			0.10	0.10
700			0.08	0.08			0.20	0.20			0.08	0.08
725			0.06	0.06			0.17	0.17			0.06	0.06
750			0.05	0.05			0.16	0.16			0.05	0.05

© Author(s) 2018

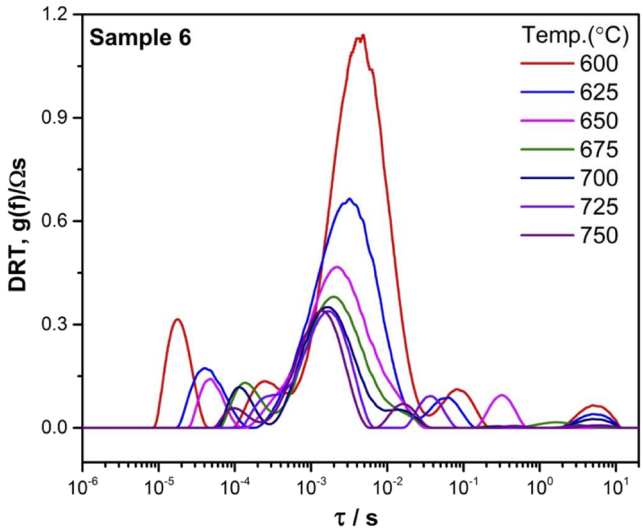


FIG. 2. Distribution of relaxation time representation of impedance spectroscopy data of sample 6 separating the low and high frequency responses.

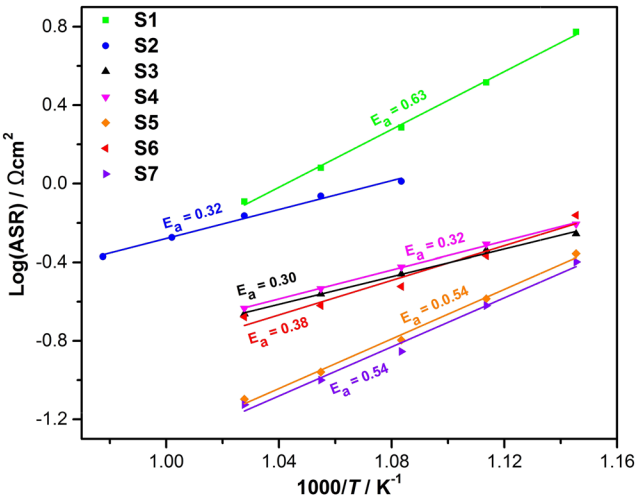


FIG. 3. Polarisation resistances versus reciprocal temperature Arrhenius plots for different cell configurations showing the thermal behavior of electrode processes.

response compared to the low-frequency response can be seen. High-frequency contributions in such materials are proposed to stem from charge transfer of oxygen ions between the cathode and the electrolyte, and the low-frequency contribution stems from the molecular oxygen dissociation process.[23–26] The minor contributions as revealed by DRT analysis could not be identified and will need further experimental work such as impedance measurements under varying pO_2. Nevertheless, it is noteworthy and signifies the importance of adding an LSGM interlayer and ball milling the electrode material in order to reduce the interfacial resistance contribution to overall polarisation resistance. It becomes clear when we compare these results to our previous investigations of the $La_2Pr_2Ni_3O_{9.65}$ composition, wherein an interlayer was not used; it was observed that the poor adherence of $La_2Pr_2Ni_3O_{9.65}$ to the electrolyte pellet was responsible for the charge transfer process being the rate-limiting factor for the ORR and thus the major contribution to overall cell polarisation resistance.[19] The contribution of interfacial resistance to overall polarisation resistance is significantly reduced in the present case by adding the LSGM interlayer and ball-milling the electrode material. As we will see later in post-testing microstructural SEM images, the electrode/electrolyte interface improvement by adding an interlayer is indeed substantial and therefore the enhancement in cathode performance.

The normalised ASR obtained for sample 1 at a temperature of 700 °C was found to be 0.61 Ω cm^2, with an activation energy of 0.63 eV (Fig. 3). This improved to 0.53 Ω cm^2 by simply ball milling the cathode material and then triple roll milling the ink (sample 2), which further increased in terms of performance, 0.17 Ω cm^2, when the LSGM pellet used was polished (sample 3). This is interesting as intuitively one would expect better performance when the pellet used was *not* polished, providing contact points for sintering, but we observe otherwise. One possible explanation could be that total effective contact area of the electrode ink layer with the electrolyte was reduced when compared to the polished smooth pellet, because of the local roughness observed in the un-polished pellets. The next change was made by sintering the LSGM pellet again after polishing, and it was observed that it did not have a significant impact on the performance of the material, presenting an ASR of 0.18 Ω cm^2 at 700 °C. As one would expect, the polarisation resistance of samples 2-4 showed similar thermal activation behavior, with almost the same activation energy in all cases (Fig. 3). The thermal behavior of sample

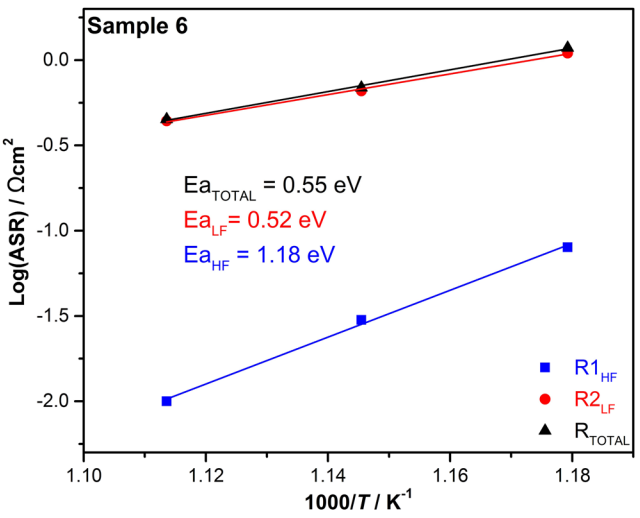


FIG. 4. Thermal activation behavior of sample 6 at low-temperatures.

© Author(s) 2018

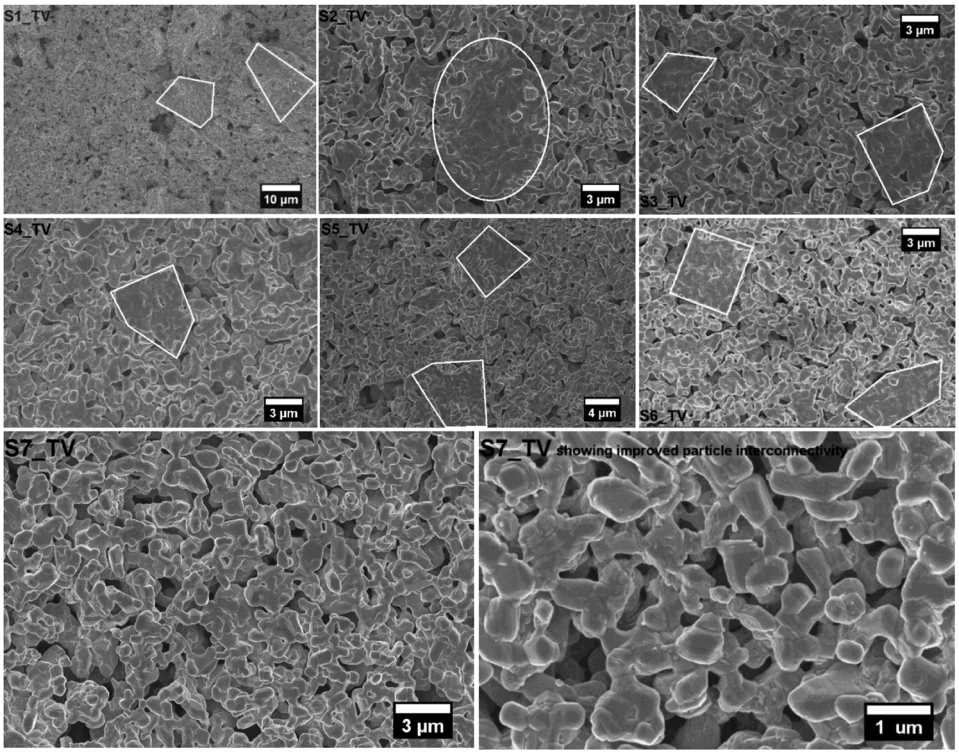


FIG. 5. Post-test microstructural SEM images showing the top view (TV) of the electrode in all samples. Sample 1 shows considerable densification, but ball milling and triple-roll milling improve the microstructure in the remaining samples. However, slight coarsening of the electrode in samples 2-6 can be observed. Reducing the sintering temperature and time in sample 7 improves the microstructure further, which is later reproduced in the electrochemical performance of the cell.

6 was further analyzed, and it was found that activation energy for the high frequency response (1.18 eV) was greater than the low frequency response (0.52 eV) (Fig. 4). Similar behavior was observed in samples 5 and 7.

The microstructure of the material showed considerable improvement when ball milled and triple-roll milled. The uniform particle size (1-3 μm) also resulted in better contact with the electrolyte pellet, which was later reflected in the half-cell

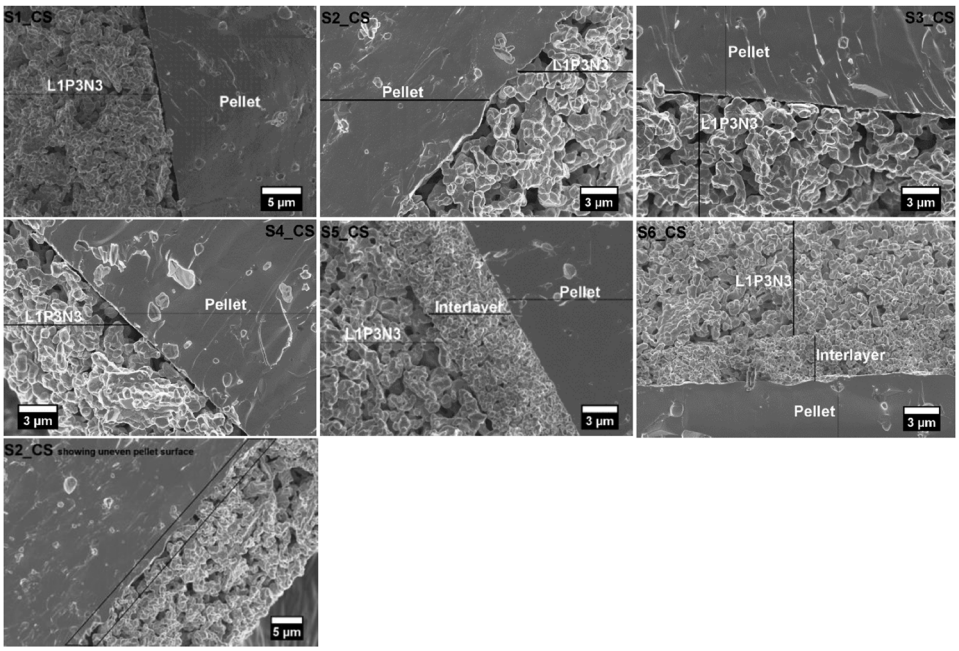


FIG. 6. Post-test microstructural SEM images showing cross-sectional (CS) views of the electrode in samples 1-6, S1_CS to S6_CS. As expected, the contact is very poor in sample. The use of an interlayer presents the best interface (samples 5 and 6). A lower magnification SEM image of sample 2 shows the uneven surface of the LSGM electrolyte leading to reduced effective electrode-electrolyte interface contact.

© Author(s) 2018

performance. In both the top and cross-sectional view of the cell, sample 1 shows considerable coarsening (>10 μm) when compared to samples 2-4 (Figs. 5 and 6). Since the ink used for samples 2-6 was the same (ink B), the top-view of the cathode after impedance measurements looks similar in these samples. Although the microstructure shows significant improvement from sample 1, two important things that stand out in samples 2-6 are the slight densification (>5 μm) in certain areas (highlighted in white outlines in Fig. 5) and the regions with poor particle interconnectivity (Fig. 5).

Densification is expected to impact the adherence of the L1P3N3 electrode to the LSGM pellet negatively and therefore the interface structure. This also explains the inferior performance of sample 1 because the substantial sintering of L1P3N3 heavily increases the interfacial resistance and thus poor cathode performance. An interesting observation, however, is the better performance of samples 3 and 4 over sample 2 when the SEM image suggests relatively better electrode-electrolyte contact to the naked eye in the latter case. This, we believe, is because the un-polished LSGM pellet used in sample 2 presents an uneven surface and thus reduces the effective electrode-electrolyte contact at the interface (Fig. 6). The top-view of sample 7 shows almost no particle growth due to cell sintering and also presents better particle interconnectivity when compared to samples 1-6, which partly explains its impressive performance (Fig. 5).

Although the ASR of 0.17 Ω cm^2 measured at 700 °C can be considered a good performance, the interface structure as revealed by SEM (S2-4, Fig. 6) in the post-test microstructural analysis showed room to further optimise the contact area. In the case of higher-order RP phases, achieving a good adherence between electrolyte and electrode has been a problem, primarily because of the decomposition of these materials at temperatures above ~1050 °C and therefore the employment of low temperatures for sintering the cells. By sintering the cells under an oxygen atmosphere, it was possible to avoid the temperature restriction imposed by the phase stability, but it was observed that the interface could still be improved. Adding an interlayer of LSGM ink before screen-printing the electrode ink onto the electrolyte pellet was therefore conceived as a route to improve the adherence of the electrode material to the electrolyte pellet. An LSGM interlayer of ~10 μm thickness, as used in sample 5, resulted in reducing the ASR to 0.08 Ω cm^2 at 700 °C. This significant improvement has been assigned mainly to the improved interface adherence. This is very clear when we examine the post-test microstructural SEM images of sample 5. The contact between the electrode and electrolyte has improved considerably and therefore the cathode performance (Fig. 6). Particle densification, however, can still be observed in sample 5, and reducing the sintering temperature to 1050 °C under oxygen atmosphere still showed particle coarsening (S6, Fig. 5). This is because of the elongated periods of time (~11-14 h) needed for the cell sintering procedure under oxygen atmosphere conditions. Therefore, an attempt was made to reduce the cell sintering time to avoid particle agglomeration and also to avoid the complex process of sintering the cell under an oxygen atmosphere. Sintering the cell at 1050 °C for only 2.5 h under ambient atmosphere reduced the electrode particle coarsening significantly (S7, Figs. 5 and 7). This is because the time for sintering the cell was reduced substantially in sample 7, and this is also reproduced in the performance of the material, presenting an ASR of 0.08 Ω cm^2 at 700 °C. The post-test microstructural SEM images (Fig. 5) in sample 7 show that there is almost no particle coarsening, improved inter-particle connectivity, and very good levels of porosity in the electrode ink. This is one of the reasons behind its superior performance, apart from the observation that the electrode adheres to the electrolyte very strongly, thereby reducing the interfacial polarisation significantly in sample 7 (Fig. 7). It is notable that this performance is a significant improvement to the one reported by Sharma *et al.* for $La_4Ni_3O_{10-\delta}$ using the spray deposition technique and showing an ASR of 0.15 Ω cm^2 at 700 °C.[17]

A new higher-order RP phase composition $LaPr_3Ni_3O_{9.76}$ was synthesised by a sol-gel route and tested for IT-SOFC

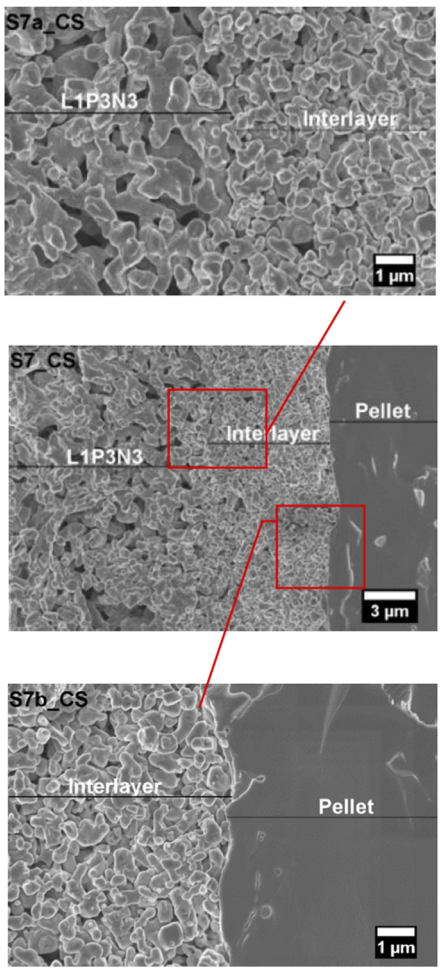


FIG. 7. Cross-sectional SEM images of sample 7 showing strong adherence of the electrode to the electrolyte pellet.

© Author(s) 2018

cathode properties. Microstructure and interface optimisation was the focus of this work, which was first achieved by ball-milling the electrode material and triple-roll milling the ink prepared, and the best performance achieved was 0.17 Ω cm^2 at 700 °C. However, the electrode adherence was still observed to be limited and thus an LSGM ink interlayer between the electrode and electrolyte was used to improve the interface contact, which produced the best performance of 0.08 Ω cm^2 at 700 °C. This significant improvement has been ascribed to the improved inter-particle connectivity, reduced densification of electrode material, and improved interface structure. It is to be noted that this is the best performance ever reported for n = 3 Ruddlesden-Popper phase materials with LSGM as an electrolyte.

See supplementary material for the powder X-ray diffraction data and X-ray photoelectron spectroscopy data of the L1P3N3 composition.

The authors would like to thank the Imperial College President's Ph.D. Scholarships and EPSRC Advanced Characterisation of Materials Centre for Doctoral Training (No. EP/L015277/1) for funding this research.

REFERENCES

[1]J. Fleig, Annu. Rev. Mater. Res. **33**, 361–382 (2003).
[2]A. Tarancon, M. Burriel, J. Santiso, S. J. Skinner, and J. A. Kilner, J. Mater. Chem. **20**, 3799–3813 (2010).
[3]A. Orera and P. R. Slater, Chem. Mater. **22**, 675–690 (2010).
[4]A. Grimaud, F. Mauvy, J. Marc Bassat, S. Fourcade, M. Marrony, and J. Claude Grenier, J. Mater. Chem. **22**, 16017–16025 (2012).
[5]S. N. Ruddlesden and P. Popper, Acta Crystallogr. **11**, 54 (1958).
[6]G. Amow and S. J. Skinner, J. Solid State Electrochem. **10**, 538–546 (2006).
[7]G. Amow, I. Davidson, and S. Skinner, Solid State Ionics **177**, 1205–1210 (2006).
[8]Z. Zhang and M. Greenblatt, J. Solid State Chem. **117**, 236–246 (1995).
[9]S. Volkov, V. Vonk, N. Khorshidi, D. Franz, M. Kubicek, V. Kilic, R. Felici, T. M. Huber, E. Navickas, G. M. Rupp, J. Fleig, and A. Stierle, Chem. Mater. **28**, 3727–3733 (2016).
[10]V. Vibhu, A. Rougier, C. Nicollet, A. Flura, S. Fourcade, N. Penin, J.-C. Grenier, and J.-M. Bassat, J. Power Sources **317**, 184–193 (2016).
[11]C. Ferchaud, J.-C. Grenier, Y. Zhang-Steenwinkel, M. M. A. van Tuel, F. P. F. van Berkel, and J.-M. Bassat, J. Power Sources **196**, 1872–1879 (2011).
[12]R. J. Woolley and S. J. Skinner, Solid State Ionics **255**, 1–5 (2014).
[13]R. J. Woolley and S. J. Skinner, J. Power Sources **243**, 790–795 (2013).
[14]S. Choi, S. Yoo, J.-Y. Shin, and G. Kim, J. Electrochem. Soc. **158**, B995–B999 (2011).
[15]S. Kim, S. Choi, A. Jun, J. Shin, and G. Kim, J. Electrochem. Soc. **161**, F1468–F1473 (2014).
[16]R. K. Sharma, M. Burriel, L. Dessemond, J.-M. Bassat, and E. Djurado, J. Power Sources **325**, 337–345 (2016).
[17]R. K. Sharma, M. Burriel, and E. Djurado, J. Mater. Chem. A **3**, 23833–23843 (2015).
[18]S. P. Jiang, J. Electrochem. Soc. **162**, F1119–F1128 (2015).
[19]M. A. Yatoo, Z. Du, H. Zhao, A. Aguadero, and S. J. Skinner, Solid State Ionics **320**, 148–151 (2018).
[20]B. Toby, J. Appl. Crystallogr. **34**, 210–213 (2001).
[21]A. C. Larson and R. B. Von Dreele, "General structure analysis system (GSAS)," Los Alamos National Laboratory Report LAUR 86–748, 2004.
[22]T. H. Wan, M. Saccoccio, C. Chen, and F. Ciucci, Electrochim. Acta **184**, 483–499 (2015).
[23]M. J. Escudero, A. Aguadero, J. A. Alonso, and L. Daza, J. Electroanal. Chem. **611**, 107–116 (2007).
[24]D. Chen, R. Ran, K. Zhang, J. Wang, and Z. Shao, J. Power Sources **188**, 96–105 (2009).
[25]F. Mauvy, C. Lalanne, J.-M. Bassat, J.-C. Grenier, H. Zhao, L. Huo, and P. Stevens, J. Electrochem. Soc. **153**, A1547–A1553 (2006).
[26]J. Peña-Martínez, D. Marrero-López, J. C. Ruiz-Morales, P. Núñez, C. Sánchez-Bautista, A. J. Dos Santos-García, and J. Canales-Vázquez, Int. J. Hydrogen Energy **34**, 9486–9495 (2009).

© Author(s) 2018